Surface & Coatings Technology 487 (2024) 131026

Contents lists available at ScienceDirect

Surface & Coatings Technology

journal homepage: www.elsevier.com/locate/surfcoat

Full length article

Temporally-resolved decomposition of $Ti_{0.12}Al_{0.21}B_{0.67}$ thin films at 1000 °C

Amir Hossein Navidi Kashani [a,*,1], Sebastian Lellig [a,b,1], Marcus Hans [a], Lukas Löfler [a], Stanislav Mráz [a], Peter Schweizer [b], Arnold Müller [c], Daniel Primetzhofer [d], Johann Michler [b], Jochen M. Schneider [a]

[a] Materials Chemistry, RWTH Aachen University, Kopernikusstr. 10, D-52074 Aachen, Germany
[b] Empa, Materials Science and Technology, Laboratory for Mechanics of Materials and Nanostructures, Feuerwerkerstrasse 39, 3602 Thun, Switzerland
[c] Labor für Ionenstrahlphysik (LIP).HPK H 32, Otto-Stern-Weg 5, 8093 Zürich, Switzerland
[d] Department of Physics and Astronomy, Uppsala University, Lägerhyddsvägen 1, S-75120 Uppsala, Sweden

ARTICLE INFO

Keywords:
Stoichiometric $(Ti,Al)B_2$
Thermal stability
Coatings
AlB_{12} formation

ABSTRACT

The thermal stability of stoichiometric $Ti_{0.12}Al_{0.21}B_{0.67}$ thin films synthesized by magnetron sputtering was investigated by vacuum annealing at 1000 °C for 1 and 3 h. The as-deposited and post-annealed films were compared regarding changes in chemical composition, phase formation, and morphology.

X-ray diffraction (XRD) data indicate the formation of a single-phase solid solution in the as-deposited $Ti_{0.12}Al_{0.21}B_{0.67}$ thin film. After annealing for 1 h, scanning transmission electron microscopy (STEM), energy-dispersive X-ray mapping (EDX), and atom probe tomography (APT) investigations reveal segregation into Al- and Ti-rich $(Ti,Al)B_2$ domains, consistent with spinodal decomposition. Furthermore, the formation of AlB_{12} with a concomitant reduction in Al concentration from 20.9 to 16.8 at. %, likely by evaporation, indicate the decomposition of Al-rich $(Ti,Al)B_2$ domains during annealing for 1 h.

Analysis of the film after annealing for 3 h shows evidence for continued spinodal decomposition as well as for further decomposition of Al-rich $(Ti,Al)B_2$ domains, leading besides the formation of AlB_{12} to a reduction in Al concentration to 12.5 at. % by Al evaporation. The observed phase formation trend during *in situ* transmission electron microscopy (TEM) studies at 1100 °C is consistent with the above discussed decomposition processes. The here identified thermal stability limit, revealed with spatially resolved structure and composition probes, confines the application temperature range of $Ti_{0.12}Al_{0.21}B_{0.67}$ in vacuum to temperatures <1000 °C and underlines that thermal stability investigations solely based on XRD data result in an overestimated thermal stability.

1. Introduction

Transition metal diborides are currently considered as coating materials for applications that require remarkable durability in challenging environments and under extreme conditions, while retaining phase stability. Particularly, TiB_2 has garnered significant attention due to its high melting point, exceeding 3225 ± 20 °C [1], low density of 4.1 to 4.5 g/cm^3 [2–4], superior hardness of 45 up to 60 GPa [5–8] and an elastic modulus (Young's modulus) range of 520 to 605 GPa [5–8]. Interestingly, quantum mechanical calculations predict elastic modulus values ranging from 582 [9] to 679 GPa [10]. TiB_2 crystallizes in the AlB_2 structure, a layered arrangement of covalent, ionic bonds between Ti and B atoms resulting in the notable thermal and mechanical stability of TiB_2 [11]. Given its unique combination of properties, TiB_2 bulk materials as well as thin films are commonly utilized for wear and corrosion protection [6,12–14]. TiB_2 thin films serve as diffusion barriers in the field of microelectronics [15–18]. Bulk TiB_2 cathodes are investigated as a replacement for graphite cathodes in an effort to reduce CO_2 emissions during electrolytic Al extraction [19,20].

In a theoretical study, Alling et al. [21] investigated several AlB_2 type ternary diborides regarding mixing energetics and age hardening potential. For $(Ti_{1-x}Al_x)B_2$, a strong driving force for isostructural

* Corresponding author.
E-mail addresses: navidi@mch.rwth-aachen.de (A.H. Navidi Kashani), lellig@mch.rwth-aachen.de (S. Lellig), hans@mch.rwth-aachen.de (M. Hans), loefler@mch.rwth-aachen.de (L. Löfler), mraz@mch.rwth-aachen.de (S. Mráz), peter.ps.schweizer@outlook.com (P. Schweizer), arnold.mueller@phys.ethz.ch (A. Müller), daniel.primetzhofer@physics.uu.se (D. Primetzhofer), johann.michler@empa.ch (J. Michler), schneider@mch.rwth-aachen.de (J.M. Schneider).
[1] Contributed equally as first authors.

https://doi.org/10.1016/j.surfcoat.2024.131026
Received 30 April 2024; Received in revised form 5 June 2024; Accepted 14 June 2024
Available online 15 June 2024
0257-8972/© 2024 The Authors. Published by Elsevier B.V. This is an open access article under the CC BY-NC license (http://creativecommons.org/licenses/by-nc/4.0/).

Table 1
Chemical composition of the as-deposited and annealed $Ti_{0.12}Al_{0.21}B_{0.67}$ thin films at 1000 °C up to 3 h obtained by ERDA. While the composition of the as-deposited thin film was reported previously [29], the data is given here again for comparison. Also, the composition of the thin film deposited onto the heating chip is given in the last line.

	Ti [at. %]	Al [at. %]	B [at. %]	O [at. %]
As-deposited [29]	11.4 ± 1.2	20.9 ± 2.1	65.5 ± 3.3	2.2 ± 0.1
1 h anneal	11.7 ± 1.4	16.8 ± 2.0	67.9 ± 3.4	3.6 ± 0.2
3 h anneal	12.0 ± 1.8	12.5 ± 1.8	71.5 ± 3.6	4.0 ± 0.2
As-deposited on chip	11.9 ± 0.9	27.6 ± 2.1	59.9 ± 3.0	0.6 ± 0.0

clustering and hence the formation of Al- and Ti-rich $TiAlB_2$ regions has been predicted at 1000 °C. The authors suggested that this material system may be suitable for hard coating applications, since its potential for age hardening appears to be high [21].

From an equilibrium thermodynamics point of view, AlB_2 has been reported to decompose into Al and AlB_{12} at temperatures larger than 980 °C [22] and the equilibrium phase diagram of Ti-Al-B predicts the formation of a stable mixture of liquid Al, TiB_2, and AlB_{12} at temperatures ≥1000 °C [23].

Throughout this paper, we report the chemical composition measured in at. %. When citing chemical compositions, utilizing stoichiometric factors from literature, we add the at. % notation in brackets for the convenience of the reader. While the thermal stability of stoichiometric $(Ti,Al)B_2$ has not been studied systematically so far, Mockute et al. [24] investigated the structural and mechanical properties of $Ti_{1-x}Al_xB_{2+y}$ deposited by magnetron sputtering from AlB_2 and TiB_2 targets with $0.30 \leq x \leq 0.66$ and $0.07 \leq y \leq 1.22$. The indentation modulus (reduced elastic modulus) was reported from 278 GPa for Ti-rich to 106 GPa for the Al-rich thin films. Based on scanning transmission electron microscopy (STEM) and energy dispersive X-ray spectroscopy (STEM-EDX) data, the observed phase separation of $(Ti_{0.34}Al_{0.66})B_{2.07}$ ($Ti_{0.11}Al_{0.22}$ $B_{0.67}$) into Ti and Al-rich nanometer-size domains in the as-deposited state was proposed to be due to surface-initiated spinodal decomposition during deposition. The as-deposited $(Ti_{0.70}Al_{0.30})B_{3.22}$ ($Ti_{0.17}Al_{0.07}$ $B_{0.76}$) thin film, contrary to $(Ti_{0.34}Al_{0.66})B_{2.07}$ ($Ti_{0.11}Al_{0.22}$ $B_{0.67}$), was reported to form a homogeneous solid solution with no indication for decomposition in the presence of a B-rich tissue phase at the grain boundaries.

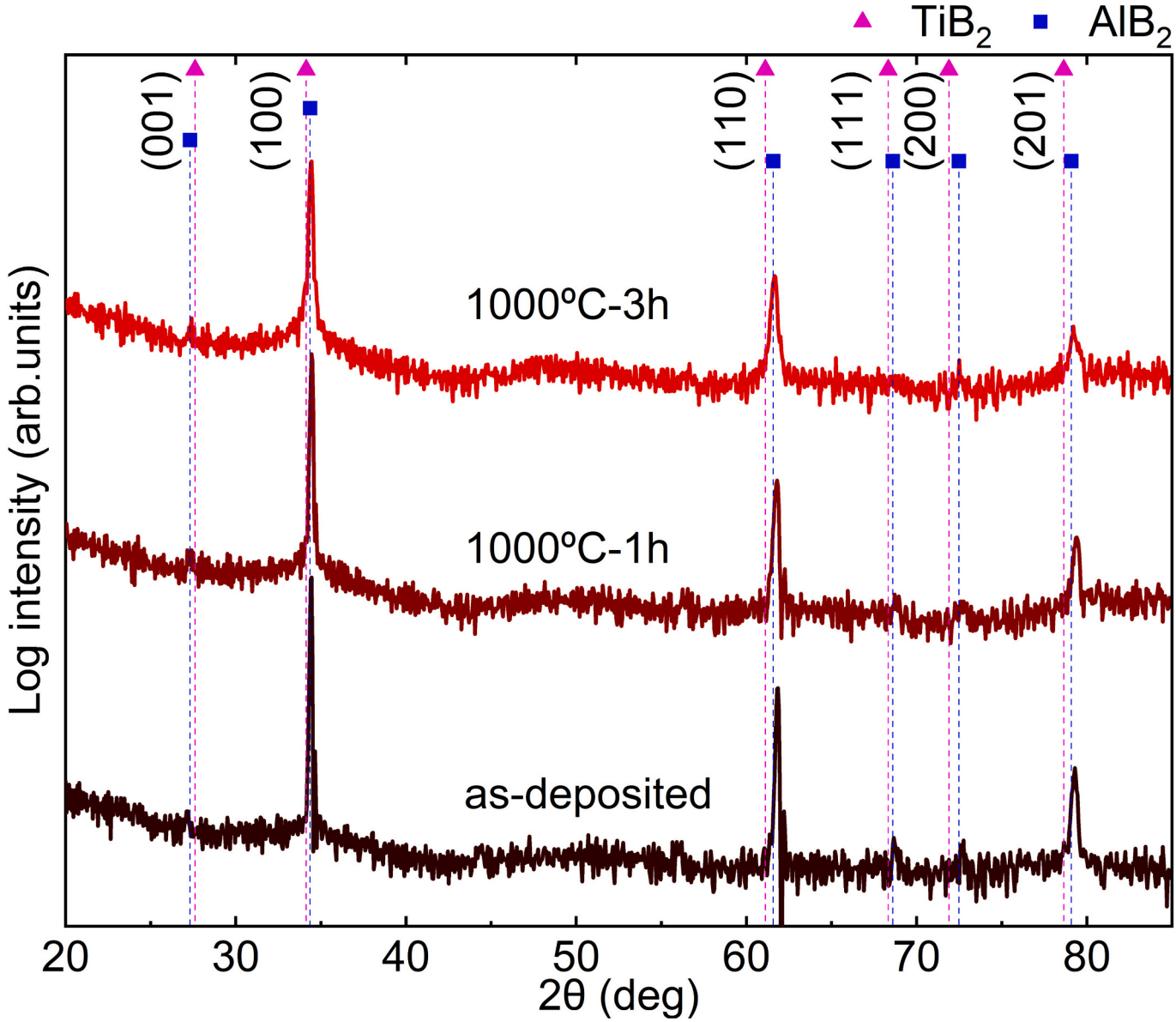

Fig. 1. Diffraction patterns of the as-deposited [29] and the annealed $Ti_{0.12}Al_{0.21}B_{0.67}$ thin films at 1000 °C for 1 and 3 h.

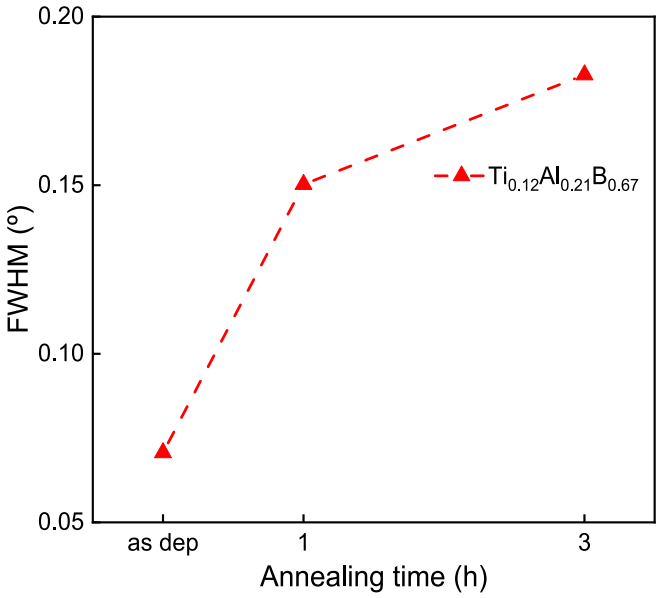

Fig. 2. FWHM of the as-deposited and annealed $Ti_{0.12}Al_{0.21}B_{0.67}$ thin films at 1000 °C as a function of the annealing time.

In another study, Mockute et al. [25] investigated the structural and mechanical properties of as-deposited and annealed thin films and reported age-hardening of DCMS deposited $(Ti_{0.71}Al_{0.29})B_{3.08}$ ($Ti_{0.17}Al_{0.07}B_{0.75}$) from AlB_2 and TiB_2 targets at 1000 °C for 1 h. The hardness and elastic modulus increased after annealing from 32 ± 0.4 to 37 ± 0.8 GPa and from 436 ± 3 to 461 ± 3 GPa, respectively. The as-deposited high hardness was attributed to a columnar microstructure, in which sub-columns of $(Ti_{0.71}Al_{0.29})B_{3.08}$ ($Ti_{0.17}Al_{0.07}B_{0.75}$) are separated by a B-tissue phase. The observed age-hardening was ascribed to the microstructural transformation within the $(Ti_{0.71}Al_{0.29})B_{3.08}$ ($Ti_{0.17}Al_{0.07}B_{0.75}$) columns and the formation of Ti-deficient $(Ti,Al)B_2$ precipitates within the grain interior. This phase separation was not attributed to spinodal decomposition, but rather to nucleation and growth [25].

From the above discussion, it is evident that thermal stability data of Ti-Al-B thin films is scarce and that the thermal stability of stoichiometric $(Ti,Al)B_2$ thin films has not been investigated systematically yet.

Here, we explore the thermal stability of stoichiometric $Ti_{0.12}Al_{0.21}B_{0.67}$ during isothermal vacuum annealing at 1000 °C for 1 and 3 h and identify the active decomposition mechanisms based on temporally and spatially resolved composition and structure analysis.

2. Experimental details

$Ti_{0.12}Al_{0.21}B_{0.67}$ thin films were grown by magnetron sputtering in a vacuum combinatorial growth deposition system with a base pressure of $<1 \times 10^{-4}$ Pa at a substrate temperature of 400 °C. Two B targets with a diameter of 50.8 mm and purity of 99.9 % (MaTecK, Germany) were sputtered using radio frequency (RF) power supplies (13.56 MHz) at power densities of 8.5 W/cm^2 and one $Ti_{0.4}Al_{0.6}$ powder-metallurgical target with diameter of 50.8 mm (Plansee Composite Materials, Germany) was sputtered using direct current (DC) power supply at power density of 2 W/cm^2. For the calculation of the power density, the whole surface area of a target (~20.3 cm^2) was considered. α-Al_2O_3 (0001) substrates were placed at 10 cm distance from the targets, rotated with a speed of 15 rpm and kept at floating potential under an Ar atmosphere (99.9999 % purity) with a pressure of 0.6 Pa. The deposition time was 180 min. The resulting deposition rate was 7.3 nm/min. The venting temperature was <50 °C. For *in situ* heating tests in the transmission electron microscopy (TEM), a Ti-Al-B thin film with ~35 nm thickness was deposited onto a Wildfire nano-chip by DENS Solutions with a Si_3N_4 membrane.

Isothermal annealing of the thin films was performed in a vacuum furnace with a base pressure of 2×10^{-4} Pa. The temperature was set to 1000 °C and the holding time was 1 and 3 h. The heating and cooling rates were set to 10 K/min.

The phase analysis of the as-deposited and annealed thin films was conducted using a Bruker AXS D8 Discover General Area Diffraction Detection System. The Cu X-ray source (λ = 0.154 nm) was operated at voltage and current of 40 kV and 40 mA, respectively, and the incidence angle was fixed at 15° to keep the information depth constant as 2 theta is varied.

The average chemical composition of the films was determined by time-of-flight elastic recoil detection analysis (ERDA) at the Tandem Accelerator Laboratory [26] of Uppsala University. 36 MeV $^{127}I^{8+}$ primary ions were used for the generation of recoils. The incidence and exit angles were 22.5° with respect to the specimen surface, while the angle between the primary ion beam and the detector telescope was 45°. The time-of-flight was measured with thin carbon foils [27] and a segmented gas detector was used [28]. The as-deposited thin film has been characterized in our previous work with a maximum total measurement uncertainty of 5 % of the deduced B concentrations as well as aliquot fractions thereof for the metals (Ti,Al) [29]. To the initial chemical composition of the thin film deposited onto the *in situ* heating chip investigated in TEM, ERDA was performed at the laboratory of Ion Beam Physics of ETH Zürich [30]. Here, $^{127}I^{7+}$ ions were used as the primary projectile with an energy of 13.5 MeV. The incidence as well as the exit angle relative to the sample surface were 18°.

Thin lamellae for TEM investigations were prepared by focused ion beam (FIB) technique using an FEI Helios Nanolab 660 dual-beam microscope with Ga^+ ions at 30 kV. As a protection layer, a 2 μm thick Pt layer was deposited using 80 pA current, followed by trench milling at 2.5 nA. The final lamellae thicknesses were <100 nm. The lamellae were subsequently analyzed by TEM using a Titan Themis 200 G3 equipped with a SuperX EDX detector (Thermo Fisher Scientific) at an acceleration voltage of 200 kV. *In situ* heating was conducted in the STEM mode and the samples were heated with an average heating rate of 12 K/min to 1100 °C and the holding time was 30 min at this temperature. The analysis of diffraction and *in situ* data was conducted with ImageJ, while Velox was used for the imaging and EDX analysis. Single out-of-focus images were removed with ImageJ in the *in situ* video for visualization.

The spatially-resolved composition at the nanometer scale of the as-deposited as well as vacuum-annealed thin films at 1000 °C for 1 and 3 h was determined by atom probe tomography (APT) using a CAMECA local electrode atom probe 4000× HR. Field evaporation was assisted by UV laser pulsing at 50 pJ pulse energy, 125 kHz pulse frequency, 60 K base temperature and the detection rate was set at 0.5 %. 0.8 to 1.4 million ions were acquired and the carried-out reconstructions with AP Suite 6.1 were based on the radii and shank angles of the as-prepared specimens. Specimens were obtained from plan-view lift-outs (see supplementary information of [31]) using FIB technique in the dual-beam microscope mentioned above according to a standard protocol [32]. Low voltage cleaning at 5 kV and 40 pA has been carried out for 10 min in order to achieve needle-like specimens with radius and shank angle of <25 nm and <10°, respectively.

3. Results and discussion

The chemical composition of the as-deposited and annealed thin films, measured by ERDA, is displayed in Table 1. The as-deposited thin film with 11.4 ± 1.2 at. % of Ti, 20.9 ± 2.1 at. % of Al, and 65.5 ± 3.3 at. % of B is stoichiometric [29] within the measurement uncertainty and for simplicity referred to as $Ti_{0.12}Al_{0.21}B_{0.67}$ in the following discussion. The Al concentration of the as-deposited thin film decreases from 20.9 to 16.8 at. % after annealing for 1 h and to 12.5 at. % after annealing for 3 h. Meanwhile, the O concentration increases from 2.2 at.

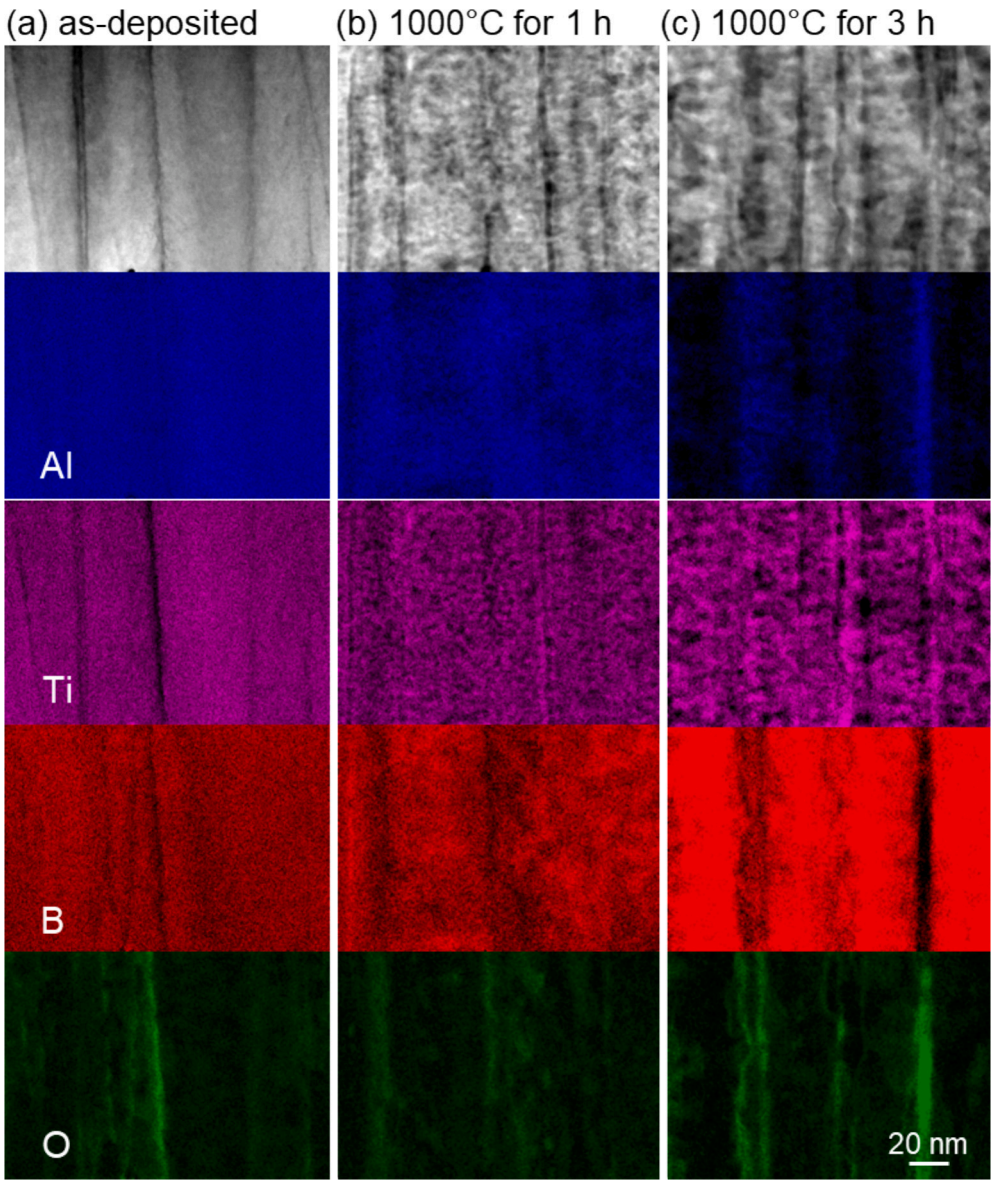

Fig. 3. STEM-HAADF images and quantified EDX elemental maps, of the (a) as-deposited and annealed $Ti_{0.12}Al_{0.21}B_{0.67}$ thin films at 1000 °C for (b) 1 h and (c) 3 h.

% for as-deposited thin film to 3.6 and 4.0 at. % after annealing for 1 and 3 h, respectively. The O concentration of the as-deposited thin film is most likely due to the incorporation of residual gas during the growth process [33,34] and/or due to reactions occurring during exposure to the atmosphere after growth [35]. The oxygen concentration of 4.0 ± 0.3 at. % in the thin film annealed for 3 h can be explained by oxygen uptake during annealing from the residual gas and/or upon exposure to the atmosphere [35]. The thin film deposited on the heating chip contains 11.9 ± 0.9 at. % of Ti, 27.6 ± 2.1 at. % of Al, 59.9 ± 3.0 at. % of B, and 0.6 ± 0.0 at. % of O.

XRD was employed to analyze the phase formation of the thin films grown on sapphire (0001) and the results are presented in Fig. 1. The TiB_2 and AlB_2 reference lines, based on [36,37], are represented by triangle and square markers, respectively. The formation of a polycrystalline single-phase hexagonal solid solution, henceforth referred to as $(Ti,Al)B_2$, is witnessed by the presence of (100), (110), (111), (200) and (201) peaks in the diffractogram of the as-deposited $Ti_{0.12}Al_{0.21}B_{0.67}$ thin film. With increasing annealing time and decreasing Al concentration, see Table 1, the intensity of the diffraction peaks decreases, see Fig. 1, and the full width at half maximum increases concomitantly, see Fig. 2. The corresponding lattice parameters of the thin films in this study can be found in the supplementary material. No evidence for the phase formation of AlB_{12}, as predicted in the equilibrium phase diagram [23], was resolvable by XRD.

Fig. 2 depicts the full width at half maximum (FWHM) [38] measured for (001), (100), (110), and (201) diffraction peaks versus annealing time. Increasing FWHM values have been reported to signal the onset of spinodal decomposition for (Ti,Al)N [38,39]. Hence, it is reasonable to assume that the here observed FWHM increase from 0.07° (as-deposited) to 0.15° (1 h anneal) and to 0.18° (3 h anneal) indicates the onset of spinodal decomposition in $Ti_{0.12}Al_{0.21}B_{0.67}$ as predicted by Alling et al. [21].

In Fig. 3, high angle annular dark field (STEM-HAADF) images with the corresponding EDX elemental maps of the as-deposited and annealed $Ti_{0.12}Al_{0.21}B_{0.67}$ thin films are shown. Fig. 3(a) displays the microstructure and elemental maps of the as-deposited thin film, in which homogenous elemental distributions of Ti, Al and B can be observed within the columns, while the intercolumnar boundaries appear to be enriched in O and Al compared to the homogenous elemental distribution within the grain. These results are in contrast with the STEM-EDX observations of Mockute et al. [24] of an as-deposited $(Ti_{0.34}Al_{0.66})B_{2.07}$ $(Ti_{0.11}Al_{0.22}\ B_{0.67})$ thin film, where surface-initiated spinodal

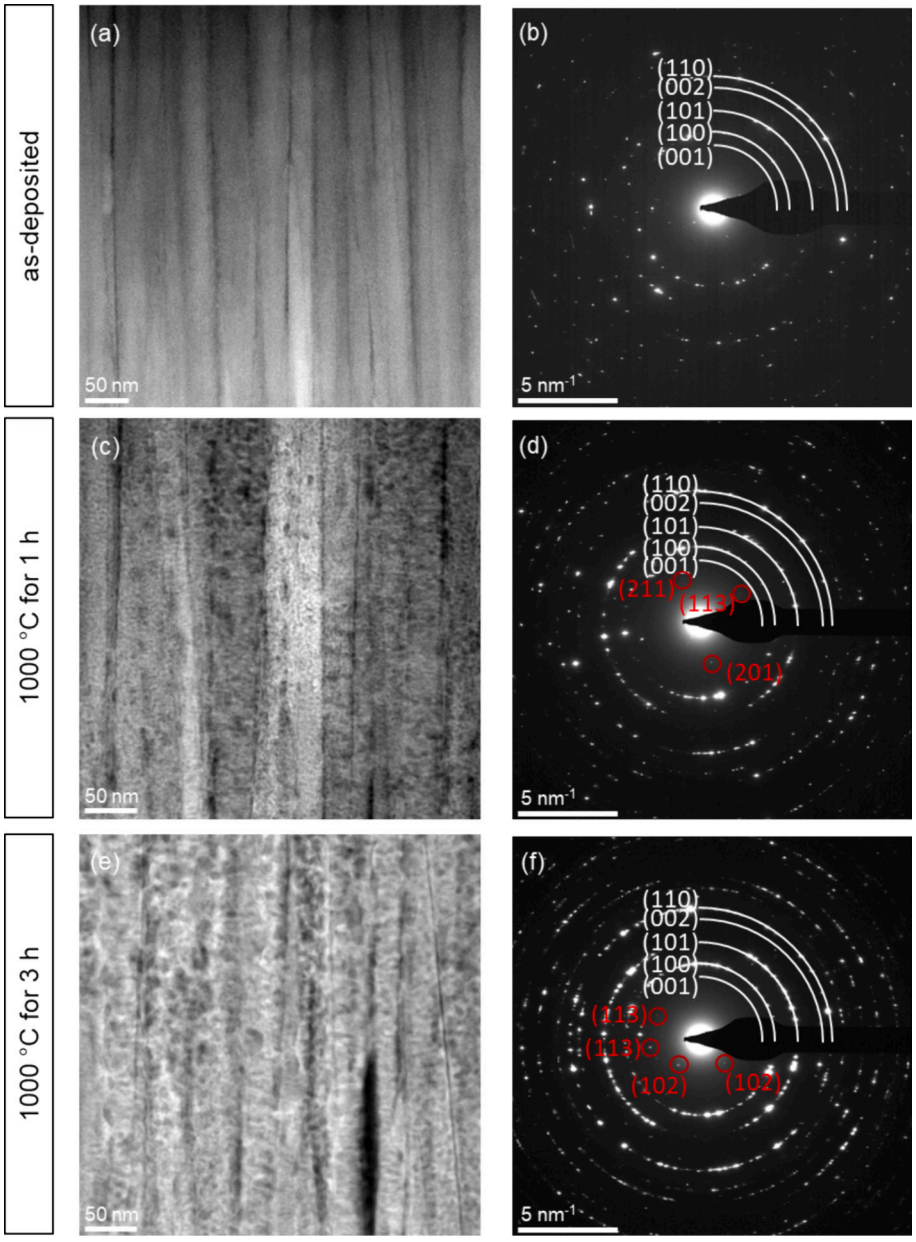

Fig. 4. STEM characterization including HAADF images and SAED patterns with peak positions for TiB_2 [36] and AlB_2 [37] (white rings) and AlB_{12} [40] (red rings). (a) and (b) for the as-deposited $Ti_{0.12}Al_{0.21}B_{0.67}$, (c) and (d) after 1 h and (e) and (f) after 3 h of annealing at 1000 °C.

decomposition and formation of Ti- and Al-rich nanometer-size domains were reported. This difference might be rationalized based on the different ion kinetic energy utilized during growth since a substrate bias potential of −50 V was applied in [24] compared to the floating substrate bias potential employed here.

After annealing for 1 h, see Fig. 3(b), Ti- and Al-rich $(Ti,Al)B_2$ domains with an extension ≤10 nm start to form in the ternary solid solution $(Ti,Al)B_2$ matrix, which is consistent with spinodal decomposition as predicted by Alling et al. [21]. After annealing for 3 h, a more pronounced segregation into Ti- and Al-rich $(Ti,Al)B_2$ domains with an extension of ≤20 nm can be observed in Fig. 3(c).

While the intercolumnar boundaries appeared to be already enriched with O and Al in the as-deposited state, see Fig. 3(a), likely due to residual gas incorporation during film growth [33] and/or during atmosphere exposure [35], the oxygen population within the intercolumnar boundaries increased after annealing, indicating the incorporation of oxygen from the residual gas, see Fig. 3(b) and (c) in comparison to (a). The spatially-resolved STEM-EDX data agree with global compositions measured by ERDA: While the oxygen concentration of the as-deposited film is 2.2 at. %, after annealing for 1 and 3 h, an increase to 3.6 and 4.0 at. % is obtained, respectively, see Table 1.

To further probe annealing induced changes in local structure, STEM imaging and selected area electron diffraction (SAED) were employed: Fig. 4(a) shows a cross-sectional image of as-deposited thin film with a columnar morphology, that is still intact after annealing at 1000 °C, see Fig. 4(c) and (e). Minute contrast differences indicate, consistent with the EDX data in Fig. 3(a), a homogeneous elemental distribution within the columns. In Fig. 4(b), the corresponding SAED pattern is indicating, consistent with the XRD data from Fig. 1, the formation of the solid solution $(Ti,Al)B_2$.

Significant contrast differences associated with chemical modulations are not visible within the columns of the as-deposited thin film, see Fig. 4(a), but appear after annealing for 1 h and intensify after the 3 h anneal, see Fig. 4(c) and (e), respectively. Based on the SAED pattern

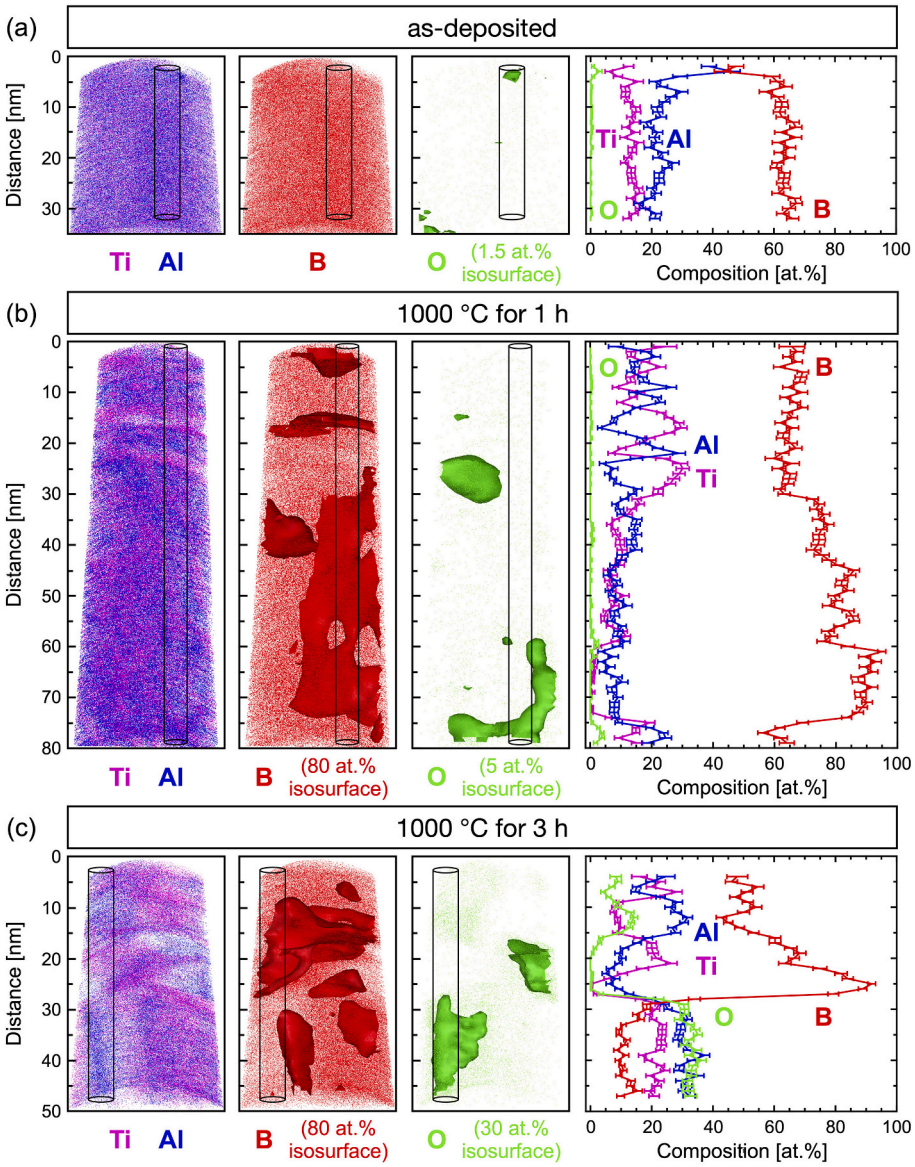

Fig. 5. Spatially-resolved composition at the nanometer scale, obtained by APT. Atomic positions and composition profiles from cylindrical regions with diameter of 5 nm are shown for (a) the as-deposited state as well as after vacuum annealing at 1000 °C for (b) 1 h and (c) 3 h. The atomic positions of Ti and Al are shown together for all panels, while B-rich regions (≥80 at. %) are highlighted by isoconcentration surfaces in (b) and (c). Isoconcentration surfaces of O-rich regions are ≥1.5 at. % in (a), ≥5 at. % in (b) and ≥30 at. % in (c).

presented in Fig. 4(d), the formation of AlB_{12} is indicated by the presence of low intensity (113), (201), and (211) AlB_{12} diffraction signals after annealing for 1 h in addition to the previously identified ternary solid solution. The presence of the solid solution $(Ti,Al)B_2$ can also be observed after annealing for 3 h, as well as another indication for AlB_{12} formation by (102) and (113) diffraction signals, see Fig. 4(f). The relatively low intensity of the AlB_{12} diffraction signals can be attributed to the small size of AlB_{12} crystallites as well as their low volume fraction in comparison to solid solution matrix. This observation is in consonance with the annealing temperature induced increase in FWHM depicted in Fig. 2 and with the notion of continuous decomposition during annealing.

Additionally, annealing induced pore formation, see Fig. 4(c) and (e), and Fig. S1, preferentially at intercolumnar boundaries and in close proximity to the substrate (see Fig. S2), can be observed. These pores exhibit widths of up to 5 nm and lengths of up to 120 nm after 1 h and widths of up to 15 nm and lengths of up to 220 nm after 3 h, while their surface appears to be enriched in oxygen, see Fig. S1, b.

The local chemical composition was further studied with APT for the as-deposited as well as the vacuum-annealed films at 1000 °C for 1 h and 3 h, see Figs. 5 and 6. The reconstructions of Ti, Al, B and O atomic positions as well as the composition profile from the cylinder of the as-deposited film presented in Fig. 5(a), reveal the presence of O-rich regions with a size of up to 4 nm and containing up to 3 at. % O. In the distance range of 5 to 35 nm the average Ti, Al and B contents are 13.7 ± 1.4 at. %, 22.2 ± 1.7 at. %, and 64.1 at. %, respectively, neglecting the average O content of <0.2 at.%. These values correspond to an Al/(Ti + Al) ratio of 0.62 ± 0.04, Fig. 6(a). However, deviations from the average values can be observed, which are larger than the measurement precision of ±2 at. %. An Al-rich region is identified in the distance range of 6 to 8 nm with 11.5 ± 1.4 at. % Ti and maximum Al content of 29.9 ± 2.0 at. %, corresponding to an Al/(Ti + Al) ratio of 0.72 ± 0.04. Also, the formation of a Ti-rich region is evident in the distance range of 28 to 30 nm with 15.6 ± 1.5 at. % Ti and minimum Al content of 15.7 ± 1.5 at. %, corresponding to an Al/(Ti + Al) ratio of 0.50 ± 0.05. The Al/(Ti + Al) ratios of 0.72 ± 0.04 (Al-rich region) and 0.50 ± 0.05 (Al-deficient

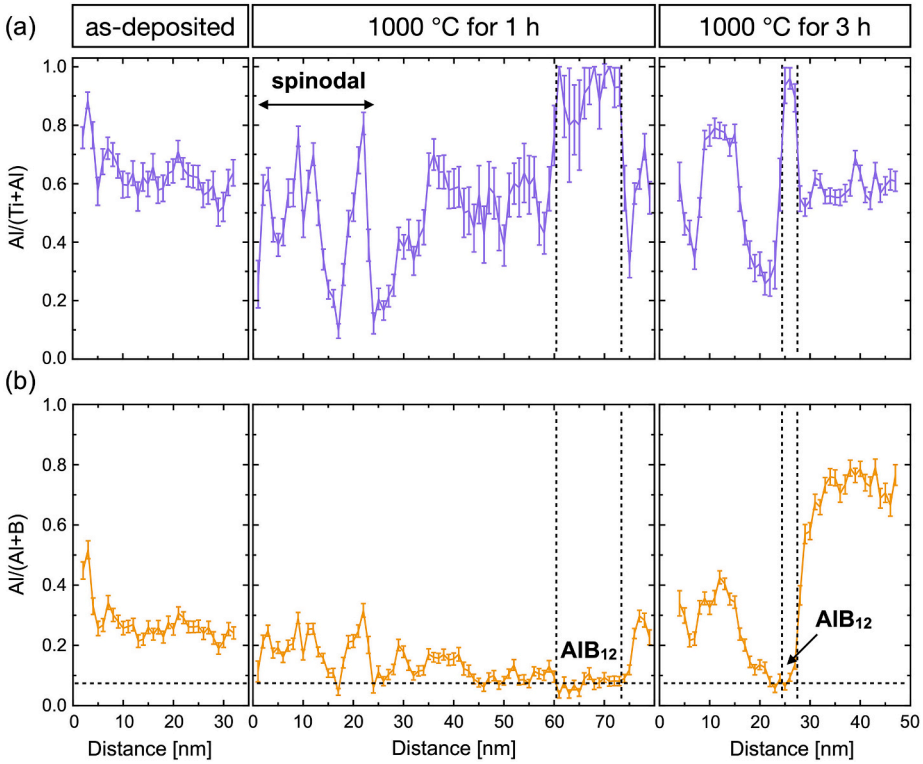

Fig. 6. Evaluation of composition profiles from Fig. 5 with respect to (a) Al/(Ti + Al) ratio and (b) Al/(Al + B) ratio. A spinodally decomposed region is highlighted with an arrow after vacuum annealing at 1000 °C for 1 h. Moreover, the local formation of AlB_{12} is emphasized with dashed lines after vacuum annealing at 1000 °C for 1 h and 3 h.

region) are significantly different from the average value of 0.62 ± 0.04, Fig. 6(a). The presence of 2 nm sized Al-rich and Ti-rich regions in the as-deposited sample may indicate the onset of surface diffusion mediated spinodal decomposition. The reconstruction of atomic positions as well as the composition profile from the cylinder region of the vacuum-annealed sample at 1000 °C for 1 h are presented in Fig. 5(b). B- and O-rich regions are highlighted by isoconcentration surfaces with ≥80 at. % B and ≥5 at. % O and most likely correspond to grain boundaries. Compositional modulations of Ti and Al in the distance range of 0 to 25 nm provide evidence for spinodal decomposition. Ti and Al vary periodically and anti-cyclically and maximum variations of the Al/(Ti + Al) ratio are in the range of 0.10 ± 0.02 and 0.81 ± 0.04, Fig. 6(a). The B-rich region in the distance range from 61 to 73 nm, Fig. 5(a), exhibits an average Al/(Ti + Al) ratio of 0.91 ± 0.07, Fig. 6(a), as well as an average Al/(B + Al) ratio of 0.07 ± 0.02, Fig. 6(b), which is consistent with local AlB_{12} formation.

Significant O incorporation can be observed after vacuum annealing at 1000 °C for 3 h, as highlighted by isoconcentration surfaces with ≥30 at. % O, Fig. 5(c). Moreover, the composition profile reveals that the Al and O contents are correlated. Based on the Al/(Ti + Al) ratio in the distance range of 0 to 25 nm, the progress of thermal decomposition is emphasized by the increased modulation wavelength of >10 nm compared to <10 nm in the sample annealed for 1 h, Fig. 6(a). This notion is consistent with the increase in FWHM from 0.15 to 0.18, see Fig. 2 and the associated discussion. The local presence of AlB_{12} can be observed in the distance range of 25 to 27 nm with an average Al/(Ti + Al) ratio of 0.93 ± 0.03, Fig. 6(a), as well as an average Al/(B + Al) ratio of 0.10 ± 0.04, Fig. 6(b).

Therefore, the APT data reveal the spinodal decomposition of $Ti_{0.12}Al_{0.21}B_{0.67}$ annealed at 1000 °C into Ti- and Al-rich $(Ti,Al)B_2$ domains and the formation of AlB_{12} phase due to the partial decomposition of formed Al-rich $(Ti,Al)B_2$ domains to AlB_{12} phase. Spinodal decomposition during vacuum annealing, the formation of AlB_{12}, and Al evaporation have not been demonstrated in the literature previously. Mockute et al. [25] observed the formation of Ti-deficient $(Ti,Al)B_2$ precipitates within the grain interior of Ti-rich $(Ti_{0.71}Al_{0.29})B_{3.08}$ ($Ti_{0.17}Al_{0.07}B_{0.75}$), annealed at 1000 °C for 1 h, which was attributed to nucleation and growth and, hence, not to spinodal decomposition. The here observed spinodal decomposition is consistent with *ab initio* predictions by Alling et al. [21] while the here observed Al evaporation can be rationalized based on the fact that the vapor pressure of Al is 1.5 × 10^{-2} Pa at 1000 °C [41]. However, the formation path of AlB_{12} remains to be identified as it could be formed via decomposition of the AlB_2 phase or via Al-rich $(Ti,Al)B_2$ domains. Hence, it is evident that relying solely on XRD data for thermal stability investigations may lead to an overestimation of its thermal stability.

Formation of AlB_{12} by annealing has not been observed in thin films so far, however, it was reported in the literature for bulk materials where a glaring discrepancy exists between values reported for peritectic reaction temperature of $AlB_2 \rightarrow AlB_{12} + Al_{(l)}$, from 956 [42] to 1500 °C [43], which could be explained by different techniques of measurement, experimental conditions and concentration of impurities in the investigated samples [42–46].

To resolve the decomposition process during the annealing, *in situ* heating experiments on a $Ti_{0.12}Al_{0.28}B_{0.60}$ coated SiN-heating chip up to 1100 °C with an average heating rate of 12 K/min and a holding time of 30 min were performed.

During the heating process, the thin film was investigated with STEM imaging and analyzed with EDX after heating (Fig. 7(a)). After holding at 1100 °C for 30 min, segregation into Ti-rich (brighter regions) and Al-rich $(Ti,Al)B_2$ regions (darker regions, green circle) can be seen in Fig. 7 (a) as well as in the temporally resolved *in situ* STEM images depicted in Fig. 7(b), (c) and (d) taken during the holding period at 1100 °C after 4, 9 and 14 min and the corresponding video in the supplementary material.

The delayed onset of segregation in the *in situ* experiments, compared

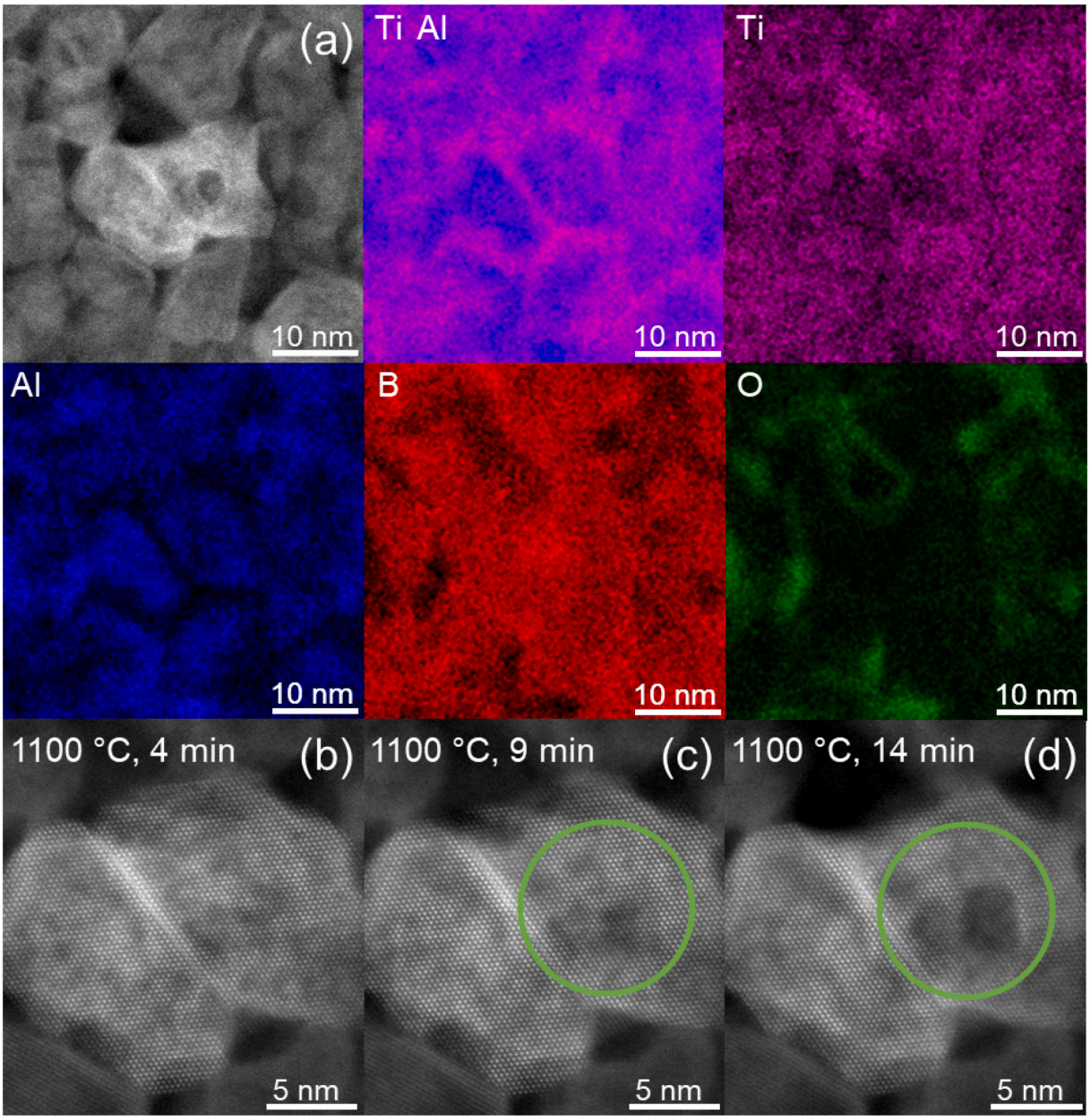

Fig. 7. HADDF image and EDX map (a) after TEM *in situ* heating at 1100 °C for 30 min. (b)-(d) during heating at 1100 °C significant segregation of Al and Ti can be observed. In the green circle, segregation into Ti- and Al-rich regions can be observed.

to the previously presented annealing data, is likely caused by the higher heating rate, lower holding time and influenced by the modified film surface chemistry by atmosphere exposure as an oxygen concentration of 8 at. % was measured by EDX, compared to the 0.6 at. % in as-deposited state, measured by ERDA. The fact that the composition of the $Ti_{0.12}Al_{0.28}B_{0.60}$ film deposited onto the heating chip was Al-rich compared to the previously discussed $Ti_{0.12}Al_{0.21}B_{0.67}$ film, cannot explain the here observed delayed decomposition as according to Alling et al. [21] the driving forces for decomposition are similar for both compositions.

4. Conclusions

We examined the thermal stability of magnetron sputtered $Ti_{0.12}Al_{0.21}B_{0.67}$ thin films by vacuum annealing at a temperature of 1000 °C for durations of 1 and 3 h. As-deposited and vacuum-annealed thin films were investigated regarding changes in chemical composition, phase formation, and morphology. XRD data of the as-deposited thin film indicated the formation of a solid solution.

After annealing for 1 h, the formation of Al- and Ti-rich $(Ti,Al)B_2$ domains, indicating spinodal decomposition, was demonstrated by STEM-EDX and APT data. Moreover, the formation of AlB_{12} with a concomitant reduction in Al concentration from 20.9 to 16.8 at. %, likely by evaporation, as a result of decomposition of Al-rich $(Ti,Al)B_2$ domains during annealing for 1 h was observed.

After annealing for 3 h, the observed phase separation was more distinct, and due to the continuous decomposition of Al-rich $(Ti,Al)B_2$ domains, the formation of AlB_{12}, confirmed by APT and SAED, and a reduction in the Al concentration to 12.5 at. %, revealed by ERDA, was observed. The observed decomposition products during *in situ* TEM heating experiments at 1100 °C were consistent with APT and SAED data at 1000 °C. Comparison with the XRD data from Fig. 1 shows that the sole reliance on XRD data for thermal stability investigation leads to an overestimation of thermal stability. Hence, the thermal stability of

$Ti_{0.12}Al_{0.21}B_{0.67}$ thin films restricts the application in vacuum to temperatures below 1000 °C.

Supplementary data to this article can be found online at https://doi.org/10.1016/j.surfcoat.2024.131026.

CRediT authorship contribution statement

Amir Hossein Navidi Kashani: Writing – review & editing, Writing – original draft, Visualization, Validation, Methodology, Investigation, Formal analysis, Data curation, Conceptualization. **Sebastian Lellig:** Writing – review & editing, Writing – original draft, Visualization, Validation, Methodology, Investigation, Formal analysis, Data curation, Conceptualization. **Marcus Hans:** Writing – review & editing, Visualization, Validation, Investigation, Formal analysis. **Lukas Löfler:** Writing – review & editing, Software, Formal analysis. **Stanislav Mráz:** Writing – review & editing, Validation, Conceptualization. **Peter Schweizer:** Writing – review & editing, Visualization, Validation, Investigation, Formal analysis. **Arnold Müller:** Writing – review & editing, Validation, Investigation, Formal analysis. **Daniel Primetzhofer:** Writing – review & editing, Validation, Resources, Investigation, Funding acquisition, Formal analysis. **Johann Michler:** Writing – review & editing, Validation, Supervision, Resources, Funding acquisition. **Jochen M. Schneider:** Writing – review & editing, Validation, Supervision, Resources, Funding acquisition.

Declaration of competing interest

The authors declare that they have no known competing financial interests or personal relationships that could have appeared to influence the work reported in this paper.

Data availability

Data will be made available on request.

Acknowledgments

This research was funded by German Research Foundation (DFG SCHN735/42-1). Accelerator operation was supported by the Swedish Research Council VR-RFI (contracts no. 2019-00191 and no. 2017-00646_9) and the Swedish Foundation for Strategic Research (contract RIF14-0053). The authors gratefully acknowledge the computing time granted by the Jülich-Aachen Research Alliance (JARA) HPC section at the IT Center of RWTH Aachen University under the projects JARA0151.

References

[1] W.G. Fahrenholtz, G.E. Hilmas, Ultra-high temperature ceramics: materials for extreme environments, Scr. Mater. 129 (2017) 94–99, https://doi.org/10.1016/j.scriptamat.2016.10.018.
[2] H. Holleck, Material selection for hard coatings, J. Vac. Sci. Technol. 4 (1986) 2661–2669, https://doi.org/10.1116/1.573700.
[3] R.G. Munro, Material properties of titanium diboride, J. Res. National Inst. Stand. Technol. 105 (2000) 709, https://doi.org/10.6028/jres.105.057.
[4] J. Thörnberg, J. Palisaitis, N. Hellgren, F.F. Klimashin, N. Ghafoor, I. Zhirkov, C. Azina, J.-L. Battaglia, A. Kusiak, M.A. Sortica, J.E. Greene, L. Hultman, I. Petrov, P.O.Å. Persson, J. Rosen, Microstructure and materials properties of understoichiometric TiB_x thin films grown by HiPIMS, Surf. Coat. Technol. 404 (2020) 126537, https://doi.org/10.1016/j.surfcoat.2020.126537.
[5] M. Berger, S. Hogmark, Evaluation of TiB_2 coatings in sliding contact against aluminium, Surf. Coat. Technol. 149 (2002) 14–20, https://doi.org/10.1016/S0257-8972(01)01361-5.
[6] M. Berger, L. Karlsson, M. Larsson, S. Hogmark, Low stress TiB_2 coatings with improved tribological properties, Thin Solid Films 401 (2001) 179–186, https://doi.org/10.1016/S0040-6090(01)01481-X.
[7] P.H. Mayrhofer, C. Mitterer, J.G. Wen, J.E. Greene, I. Petrov, Self-organized nanocolumnar structure in superhard TiB_2 thin films, Appl. Phys. Lett. 86 (2005) 131909, https://doi.org/10.1063/1.1887824.
[8] M.N. Polyakov, M. Morstein, X. Maeder, T. Nelis, D. Lundin, J. Wehrs, J.P. Best, T. E.J. Edwards, M. Döbeli, J. Michler, Microstructure-driven strengthening of TiB_2 coatings deposited by pulsed magnetron sputtering, Surf. Coat. Technol. 368 (2019) 88–96, https://doi.org/10.1016/j.surfcoat.2019.04.042.
[9] V. Milman, M.C. Warren, Elastic properties of TiB_2 and MgB_2, J. Phys. Condens. Matter 13 (2001) 5585, https://doi.org/10.1088/0953-8984/13/24/304.
[10] K.B. Panda, K.S. Ravi Chandran, Determination of elastic constants of titanium diboride (TiB_2) from first principles using FLAPW implementation of the density functional theory, Comput. Mater. Sci. 35 (2006) 134–150, https://doi.org/10.1016/j.commatsci.2005.03.012.
[11] I.R. Shein, A.L. Ivanovskii, Elastic properties of mono- and polycrystalline hexagonal AlB_2-like diborides of s, p and d metals from first-principles calculations, J. Phys. Condens. Matter 20 (2008) 415218, https://doi.org/10.1088/0953-8984/20/41/415218.
[12] M. Berger, S. Hogmark, Tribological properties of selected PVD coatings when slid against ductile materials, Wear 252 (2002) 557–565, https://doi.org/10.1016/S0043-1648(02)00011-X.
[13] A.S. Dranenko, V.A. Lavrenko, V.N. Talash, Corrosion resistance of nanostructured TiB_2 films in 3% NACl solution, Powder Metall. Met. Ceram. 49 (2010) 174–178, https://doi.org/10.1007/s11106-010-9218-4.
[14] I.I. Korobov, G.V. Kalinnikov, A.V. Ivanov, N.N. Dremova, R.A. Andrievski, S. P. Shilkin, Corrosion resistance of nanostructured films of titanium diboride in mineral acid solutions, Prot. Met. Phys. Chem. Surf. 52 (2016) 618–621, https://doi.org/10.1134/S2070205116040171.
[15] J. Shappirio, J. Finnegan, R. Lux, D. Fox, J. Kwiatkowski, H.P. Kattelus, M. A. Nicolet, TiB_2 and ZrB_2 diffusion barriers in GaAs Ohmic contact technology, J. Vac. Sci. Technol. 3 (1985) 2255–2258, https://doi.org/10.1116/1.572902.
[16] G. Sade, J. Pelleg, Co-sputtered TiB_2 as a diffusion barrier for advanced microelectronics with Cu metallization, Appl. Surf. Sci. 91 (1995) 263–268, https://doi.org/10.1016/0169-4332(95)00129-8.
[17] J.S. Chen, J.L. Wang, Diffusion barrier properties of sputtered TiB_2 between Cu and Si, J. Electrochem. Soc. 147 (2000) 1940, https://doi.org/10.1149/1.1393462.
[18] J.L. Wang, J.S. Chen, TiB_2 as a diffusion barrier for Cu/<Si> metallization, MRS Online Proc. Libr. 563 (1999) 33–38, https://doi.org/10.1557/PROC-563-33.
[19] J. Li, X.-j. Lü, Y.-q. Lai, Q.-y. Li, Y.-x. Liu, Research progress in TiB_2 wettable cathode for aluminum reduction, JOM 60 (2008) 32–37, https://doi.org/10.1007/s11837-008-0104-1.
[20] S.K. Padamata, K. Singh, G.M. Haarberg, G. Saevarsdottir, Wettable TiB_2 cathode for aluminum electrolysis: a review, Journal of Sustainable Metallurgy 8 (2022) 613–624, https://doi.org/10.1007/s40831-022-00526-8.
[21] B. Alling, H. Högberg, R. Armiento, J. Rosen, L. Hultman, A theoretical investigation of mixing thermodynamics, age-hardening potential, and electronic structure of ternary $M^1_{1-x}M^2_xB_2$ alloys with AlB_2 type structure, Sci. Rep. 5 (2015) 9888, https://doi.org/10.1038/srep09888.
[22] H.J. Becher, Über die Darstellung und Beständigkeit von Aluminiumdiborid, Z. Anorg. Allg. Chem. 308 (1961) 13–22, https://doi.org/10.1002/zaac.19613080104.
[23] V. Raghavan, Al-B-Ti (aluminum-boron-titanium), J. Phase Equilib. Diffus. 30 (2009) 610–613, https://doi.org/10.1007/s11669-009-9585-z.
[24] A. Mockute, J. Palisaitis, N. Nedfors, P. Berastegui, E. Broitman, B. Alling, L. Å. Näslund, L. Hultman, J. Patscheider, U. Jansson, P.O.Å. Persson, J. Rosen, Synthesis and characterization of $(Ti_{1-x}Al_x)B_{2+\Delta}$ thin films from combinatorial magnetron sputtering, Thin Solid Films 669 (2019) 181–187, https://doi.org/10.1016/j.tsf.2018.10.042.
[25] A. Mockute, J. Palisaitis, B. Alling, P. Berastegui, E. Broitman, L.Å. Näslund, N. Nedfors, J. Lu, J. Jensen, L. Hultman, J. Patscheider, U. Jansson, P.O.Å. Persson, J. Rosen, Age hardening in $(Ti_{1-x}Al_x)B_{2+\Delta}$ thin films, Scr. Mater. 127 (2017) 122–126, https://doi.org/10.1016/j.scriptamat.2016.09.021.
[26] P. Ström, D. Primetzhofer, Ion beam tools for nondestructive in-situ and in-operando composition analysis and modification of materials at the Tandem Laboratory in Uppsala, J. Instrum. 17 (2022) P04011, https://doi.org/10.1088/1748-0221/17/04/P04011.
[27] Y. Zhang, H.J. Whitlow, T. Winzell, I.F. Bubb, T. Sajavaara, K. Arstila, J. Keinonen, Detection efficiency of time-of-flight energy elastic recoil detection analysis systems, Nucl. Instrum. Methods Phys. Res. Sec. B 149 (1999) 477–489, https://doi.org/10.1016/S0168-583X(98)00963-X.
[28] P. Ström, P. Petersson, M. Rubel, G. Possnert, A combined segmented anode gas ionization chamber and time-of-flight detector for heavy ion elastic recoil detection analysis, Rev. Sci. Instrum. 87 (2016) 103303. https://aip.scitation.org/doi/abs/10.1063/1.4963709.
[29] A.H. Navidi Kashani, S. Mráz, D.M. Holzapfel, M. Hans, L. Löfler, P. Ondračka, D. Primetzhofer, J.M. Schneider, Synthesis and oxidation behavior of $Ti_{0.35}Al_{0.65}B_y$ ($y = 1.7–2.4$) coatings, Surf. Coat. Technol. 442 (2022) 128190, https://doi.org/10.1016/j.surfcoat.2022.128190.
[30] C. Kottler, M. Döbeli, F. Glaus, M. Suter, A spectrometer for low energy heavy ion ERDA, Nucl. Instrum. Methods Phys. Res. Sec. B 248 (2006) 155–162, https://doi.org/10.1016/j.nimb.2006.02.013.
[31] M. Hans, Z. Czigány, D. Neuß, J.A. Sälker, H. Rueß, J. Krause, G.K. Nayak, D. Holec, J.M. Schneider, Probing the onset of wurtzite phase formation in (V,Al)N thin films by transmission electron microscopy and atom probe tomography, Surf. Coat. Technol. 442 (2022) 128235, https://doi.org/10.1016/j.surfcoat.2022.128235.
[32] K. Thompson, D. Lawrence, D.J. Larson, J.D. Olson, T.F. Kelly, B. Gorman, In situ site-specific specimen preparation for atom probe tomography, Ultramicroscopy 107 (2007) 131–139, https://doi.org/10.1016/j.ultramic.2006.06.008.
[33] J.M. Schneider, K. Larsson, J. Lu, E. Olsson, B. Hjörvarsson, Role of hydrogen for the elastic properties of alumina thin films, Appl. Phys. Lett. 80 (2002) 1144–1146, https://doi.org/10.1063/1.1448389.
[34] M. Mikula, B. Grančič, P. Švec, T. Roch, M. Truchlý, O. Kohuľák, L. Satrapinskyy, T. Fiantok, V. Izaii, M. Haršáni, Ľ. Orovčík, P. Kúš, Thermally-induced structure

evolution in ternary Ti1−xYxB2+Δ films, Scr. Mater. 164 (2019) 91–95, https://doi.org/10.1016/j.scriptamat.2019.01.042.
[35] G. Greczynski, S. Mráz, L. Hultman, J.M. Schneider, Venting temperature determines surface chemistry of magnetron sputtered TiN films, Appl. Phys. Lett. 108 (2016) 041603, https://doi.org/10.1063/1.4940974.
[36] JCPDS International Centre for Diffraction Data, Titanium Diboride (TiB_2) card 00-035-0741.
[37] JCPDS International Centre for Diffraction Data, Aluminium Diboride (AlB_2) card 00-008-0216.
[38] M. to Baben, M. Hans, D. Primetzhofer, S. Evertz, H. Ruess, J.M. Schneider, Unprecedented thermal stability of inherently metastable titanium aluminum nitride by point defect engineering, Mater. Res. Lett. 5 (2017) 158–169, https://doi.org/10.1080/21663831.2016.1233914.
[39] D.M. Holzapfel, D. Music, M. Hans, S. Wolff-Goodrich, D. Holec, D. Bogdanovski, M. Arndt, A.O. Eriksson, K. Yalamanchili, D. Primetzhofer, C.H. Liebscher, J. M. Schneider, Enhanced thermal stability of (Ti,Al)N coatings by oxygen incorporation, Acta Mater. 218 (2021) 117204, https://doi.org/10.1016/j.actamat.2021.117204.
[40] JCPDS International Centre for Diffraction Data, Aluminum dodecaboride (AlB_{12}) card 01-076-1235.
[41] C.B. Alcock, V.P. Itkin, M.K. Horrigan, Vapour pressure equations for the metallic elements: 298–2500K, Can. Metall. Q. 23 (1984) 309–313, https://doi.org/10.1179/cmq.1984.23.3.309.
[42] A. Hall, J. Economy, The $Al_{(L)} + AlB_{12} \leftrightarrow AlB_2$ peritectic transformation and its role in the formation of high aspect ratio AlB2 flakes, J. Phase Equilib. 21 (2000) 63–69, https://doi.org/10.1361/105497100770340435.
[43] E. Sirtl, L.M. Woerner, Preparation and properties of aluminum diboride single crystals, J. Cryst. Growth 16 (1972) 215–218, https://doi.org/10.1016/0022-0248(72)90204-7.
[44] C.E. Campbell, U.R. Kattner, A thermodynamic assessment of the Ni-Al-B system, Journal of Phase Equilibria 20 (1999) 485, https://doi.org/10.1361/105497199770340743.
[45] D. Mirković, J. Gröbner, R. Schmid-Fetzer, O. Fabrichnaya, H.L. Lukas, Experimental study and thermodynamic re-assessment of the Al–B system, J. Alloys Compd. 384 (2004) 168–174, https://doi.org/10.1016/j.jallcom.2004.04.100.
[46] H. Duschanek, P. Rogl, The Al-B (aluminum-boron) system, Journal of Phase Equilibria 15 (1994) 543–552, https://doi.org/10.1007/BF02649415.